

Experimental and numerical study of a shunt structure for large dynamic strain measurement

Tieyu Gao¹ and Qingfeng Xia^{2*}

Abstract—Cost-effective and energy-saving sensor for large dynamic strain measurement is still lacking for wireless sensor networking application. In this paper, a shunt structure is proposed to measure large dynamic strain using metal foil strain gauge without fatigue failure. This shunt structure is made of single metal sheet for convenient installation. The working principle of the strain shunt with one shunt sheet bridging two strain relieving units is illustrated. The strain measured on the shunt sheet surface is proportionally lower than that on the target surface where the strain shunt is attached, and the ratio of strain level reduction is derived analytically from shunt structure dimension. The constancy and stability of the shunt ratio is validated through tensile and bending load tests for both static and dynamic loads. Furthermore, the stress concentration and shunt ratio sensitivity to compound load are investigated numerically.

Index Terms—Strain gauge; shunt; fatigue failure; large strain; SHM; clip gauge; wireless sensor network

1 INTRODUCTION

Condition Based Monitoring (CBM) systems are becoming a more important and affordable tool for running machine in an optimal manner. For example, condition monitoring (CM) and structural health monitoring (SHM) systems for an offshore wind turbine system is critical for health assessment of the asset [1], minimising downtime and reducing huge maintenance and logistics impact [2, 3]. CM and SHM for a large scale off-shore wind turbine require robust sensors that can provide operational information continuously for long duration in a challenging environment. Modern mega-structures like off-shore wind turbines and oil drilling rigs must survive large dynamic strain incurred by wind or other alternating load. Due to the less accessibility of off-shore structures and high maintaining cost, the long-term reliability of force sensors is crucial. The reliability of such force sensors is mainly constrained by the fatigue life of sensors under large dynamic load and the quality of power supply and communication link. However, the existent commercial available force sensors, such as fibre Bragg grating (FBG), vibration wire, metallic foil strain gauge, do not address the challenge of fatigue failure. Having in mind of the challenges of force sensor availability for off-shore structures, this paper highlights the significance of developing innovative force sensors that can survive the large dynamic strain for long duration.

Metallic foil resistive strain gauges have been extensively used in force instruments such as weight scale, torque meter. Metallic foil strain gauge is advantageous for excellent linearity, voltage output signal, compactness, low cost, etc. However, normal resistive foil strain gauges are not suitable to measure extremely large static strain or large dynamic strain measurement in long term, due to gauge breakage or limited fatigue lifetime. Although the metallic foil strain gauge can measure static strain up to 5% [4], the typical dynamic strain measurement range for resistive strain gauge is 1600 $\mu\epsilon$ for 10^6 alternating load cycles, according to S-N fatigue curve of Vishay WK series strain gage [5].

On the other hand, the fibre Bragg grating (FBG) based optical strain gauge has the advantages of immunity to electromagnetic interference (EMI), intrinsic safety in highly explosive atmospheres, good resistance to large strain and alternating load [4], and better performance in zero-drifting [6]. Despite various advantages of FBG force sensors, they are not superior to the conventional metal foil strain gauges, with respect to measurement range of dynamic strain and precision [6]. Test of FBG on wind turbine blade shows the optical fibre strain gauge has the resolution of 1 $\mu\epsilon$ and accuracy of 5 $\mu\epsilon$, and the maximum strain level is only 1000 $\mu\epsilon$ at the 10^7 cycles [6]. Besides the significant temperature dependency, FBG strain sensors need expensive, and energy-thirsty optical equipment to detect the shifting of wavelength precisely [7]. Although using low power LED light sources and photodetectors can reduce the power consumption for the wireless sensor node [8], the battery-powered sensor can not satisfy the requirement for the long-term usability.

In addition to metallic foil and fibre optical strain gauge, novel strain-sensitive material [9] and image processing based methods are developed for large strain measurement. Strain-sensitive material like polymer optical fibre has the potential to measure large strain, surpassing the intrinsic maximum strain level (approximately 4%) of silicon fibre optical FBG sensors limited by the failure strain of silica [10]. Piezoelectric strain sensor has excellent sensitivity and performance for highly dynamic strain, but the zero-drift issue makes it for unsuitable for static strain measurement [11]. Clip gauge and extensometer are widely employed in tensile load test, but they are designed for single direction static large strain measurement. Some other image processing methods for the large strain measurement are based on the high resolution digital camera. Digital image correlation of speckle pattern on the target surface is ideal to measure large static strain on a large area [12]. Interferometry based solution, such as shearography, is capable of full field strain measurement with dedicate optical arrangement [13]. However, these optical solutions may be restricted by non-vibratory condition, as well as high power consumption and equipment cost. Thereby, they are excluded from massive deployment in industrial scenarios; in particular, off-shore platforms condition monitoring and structural health monitoring.

Currently, commercial optical or resistive strain measurement techniques are not yet available for large and dynamic strain measurement which is required by the long-

• 1School of Energy & Power Engineering, Xi'an Jiaotong University, Xianning West Road, Xi'an, 711400, China. Email: sunmoon@mail.xjtu.edu.cn

• 2*Department of Engineering Science, University of Oxford, Parks Road, Oxford, OX1 3PJ, United Kingdom. E-mail: qingfeng.xia@eng.ox.ac.uk

term structural health monitoring (SHM) and condition monitoring systems, e.g. wireless force sensing on rotating machines. One of the technical challenges is sensor failure due to large dynamic strain and sustainable power supply for wireless sensor nodes. Metallic thin film strain gauges are subject to fatigue or breakage failure at heavy alternating loads, while the higher power consumption for the FBG optical system and wavelength shift measurement are prohibiting for battery-powered wireless sensor networks. Metal foil gauge may be applied on low strain region or preloaded structure to capture strain variation.

To meet these challenges of long-term availability of wireless sensors for large dynamic strain measurement, an innovative strain shunt design is proposed to reduce the strain proportionally to a manageable level for the metallic thin film strain gauges. Combined with the advantages of metallic resistive strain gauges, this strain shunt design offers a compact, precise, cost-effective and energy-saving large strain measurement solution which is ideal for wireless sensor node powered by battery and energy harvester [14]. The strain shunt design can measure large alternating strain or displacement, in contrast to single direction measurement of clip gauge. Metal sheeting process aims at simplified manufacturing, relieved stress concentration by the fillet structures and convenient installation. Furthermore, strain shunt can apply to dynamic gap/crack width measurement, since the shunt ratio is adjustable by varying the key geometry parameters like thickness and height.

In this paper, the working principle of the strain shunt structure made of single metal sheet is illustrated and the shunt ratio is derived from a simplified 1D model. The newly designed strain shunt structure is experimentally validated through tensile and bending test. Moreover, the dynamic response of the strain shunt structure is investigated analytically and experimentally. In addition, finite element analysis (FEA) is conducted to investigate the stress concentration and the response of compound load.

II SCHEMATIC AND THEORETICAL ANALYSIS

A Principles of Strain Shunt

This shunt structure made of single piece thin metal sheet consists of several functional units, a shunt sheet bridging two strain relieving units (supporting cantilevers in this study) and two binding feet which bond the shunt structure firmly onto the target surface. If the supporting cantilevers are perfect rigid bodies without any deflective deformation, the strain on the shunt sheet is equal to that of the target surface. However, the supporting cantilevers behave as a cantilever beam with one end fixed onto the target surface and the other end under bending force. Due to the elastic response of the cantilever under bending load, the cantilevers' deflection relieves the strain level on the shunt sheet. The not-to-scale deformation of the shunt structures are demonstrated for both compressive and tensile load in Fig. 1 (b-c). The fillet structure derived from metal sheeting process can relieve stress concentration at the joint of the shunt structure and the target surface. Instead of welding

directly onto the target surface [15], binding feet are introduced for convenient integration with the target surface.

The deformation due to purely bending load is slightly different from the case of tensile or compressive load, but the relieved strain level is expected for the current shunt sheet design, shown in Fig. 1 (d). For the target surface under purely bending load, no strain is expected on the neutral plane of the target beam, and strain on the beam surface is proportional to the distance to the neutral plane $h/2$ and deflection angle θ . The shunt sheet tends to expand into length L_s' , if the supporting cantilevers are rigid. As the supporting cantilevers are designed to be flexible to accommodate most of deformation, the strain level on the shunt sheet (marked in green) could be less than on the target surface underneath (marked in red).

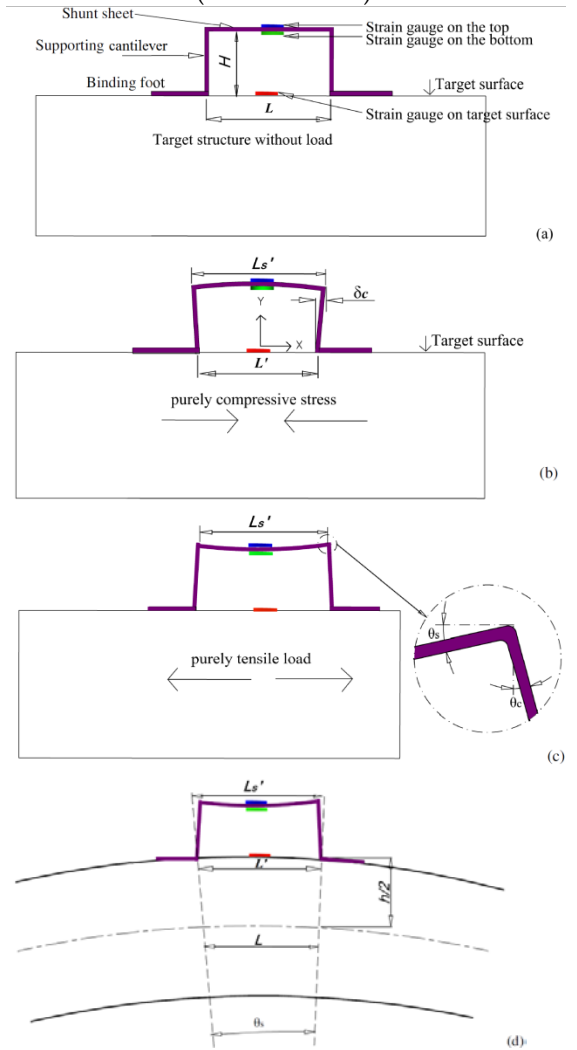


Fig. 1 Schematic of strain shunt structure under (a) no load; (b) purely compressive load; (c) purely tensile load; (d) purely bending load

It is the objective of shunt structure that the strain magnitude on the shunt sheet surface is proportionally smaller than the strain on the target surface. The working principles are illustrated via one-dimension analytical solution of the three-beam structure under purely compressive/tensile load. The following relationship for deformation along the load direction is proposed,

$$\delta_i = L\varepsilon_i = 2\delta_c + \delta_s \quad (1)$$

where L is the distance between two supporting cantilevers which is equal to the length of shunt sheet bridging; the fillet transition is ignored in this 1D analysis; δ_i is the deformation

of the target surface across L ; ε_i is the strain on the target surface beneath the shunt structure; δ_c is the deformation of each supporting cantilever and δ_s is deformation of shunt sheet in the same direction with δ_i on the target surface. The deformations discussed are all one-dimensional, across the span of the two supporting cantilevers.

Assuming homogenous strain distribution on the shunt sheet's neutral plane, the shunt ratio is defined as,

$$r_s \text{ (Shunt ratio)} = \frac{\delta_s}{\delta_i} = \frac{L\varepsilon_s}{L\varepsilon_i} \quad (2)$$

B Analytical Derivation

The shunt ratio can be derived from the 1D simplified model of supporting cantilevers and shunt sheet. The deflective deformation of cantilevers δ_{Euler} , is estimated by the flexural deformation according to Euler beam theory for slender beams [16].

$$\delta_{Euler} = \frac{FH^3}{3E_c I_c} \quad (3)$$

where E_c is the elastic modulus of the supporting cantilever; F is the tensile or compressive force on the shunt sheet applying on the non-fixed end of the supporting cantilever; H is the height of the cantilevers; $I_c = b^3w/12$ is the second moment of area for z-axis of the cantilevers, where b is the thickness and w is width of shunt structure.

However, the bending deformation is under-estimated for short cantilevers, according to Timoshenko' beam theory. The shearing strain parallel to the central plane should not be neglected, and there is a derivative equation to estimate the deformation for supporting beams with rectangular cross-section [17]. Notably, there is deformation in another direction (y axis), but it does not affect the shunt ratio.

$$\delta_x = \frac{F}{6EI} \left[3vy^2(H-y) + \frac{10yw^2}{(12+11v)} + (3H-y)y^2 \right] \quad (4)$$

where y is the coordination along the cantilever beam.

Since the bending load is acting at the top of the cantilever, the deformation at the load end ($y=H$) can be simplified to,

$$\delta_c = (1 + r_c)\delta_{Euler} \text{ where } r_c = \frac{10b^2}{(12+11v)H^2} \quad (5)$$

where r_c is the ratio to correct the under-estimated cantilever deformation given by Euler beam theory. The ratio r_c depends on the Poisson ratio of the material and H/b (slenderness of cantilever). If $H/b \gg 1$, the beam can be regarded as Euler beam, then $r_c = 0$.

The deformation of the shunt sheet caused by the tensile or compressive force F , is represented as δ_s . In addition, the warping of the shunt sheet which may lead to shrinkage or expansion in the horizontal x axis coordination is denoted as δ_w

$$\delta_s = L\varepsilon_s + \delta_w \quad (6)$$

$$\varepsilon_s = \frac{F}{A_s E_s} \quad (7)$$

where A_s is cross-section area for the shunt sheet; E_s is the elastic modulus for the shunt sheet.

Shunt ratio can also been represented in equation (8), as x-axis deformation on the central plane which is not affected by the shunt sheet warping δ_w :

$$r_s = \frac{\delta_s}{\delta_i} = \frac{L\varepsilon_s}{L\varepsilon_i} = \frac{\varepsilon_s}{\varepsilon_i} \quad (8)$$

where ε_s is the stress on the neutral plane of the shunt sheet which can be calculated as the average of the top surface centre and the bottom surface centre of the shunt sheet.

C Warping Effect

Since the joint of supporting cantilevers and the shunt sheet is not hinged in the current design, the deflection of the cantilevers results in warping of the shunt sheet connecting them. Thus, the strain distribution on the upper and lower surfaces is not homogenous due to the warping effect by the bending moment at both ends. Measurement of averaged strain on shunt sheet needs two strain gauges on both upper and lower surface, shown in Fig. 1.

As the moment acting on the shunt sheet is not known, the warping angle θ_s may be derived from the flexural angle of the cantilever θ_c . It is assumed the angle between the cantilever top surface and the shunt sheet remains constant angle during deformation, demonstrated in Fig. 1 (b). In practice, warping angle θ_s is smaller than the flexural angle of the cantilever θ_c , but the warping angle of the shunt sheet is approximated to that of deflection angle of the supporting cantilever at the joint:

$$\theta_s = f(\theta_c) \approx \theta_c \quad (9)$$

Furthermore, the deflection angle on the top of cantilever θ_c can be derived from Euler beam theory for cantilever with one end fixed and the other end under bending force,

$$\theta_c = \frac{FH^2}{2E_c I_c} \quad (10)$$

The shunt sheet is modelled as beam fixed on both sides, and the bending moment M_s acting on both ends of the shunt sheet is related to the deflection angle θ_s . Given the large ratio of length to thickness for the shunt sheet, classic Euler beam theory can be used to calculate shunt sheet warping angle due to the moment M_s acting at both ends,

$$\theta_s = \frac{M_s L}{E_s I_s} \quad (11)$$

According to the geometrical relationship in equation (9), the bending moment M_s can be derived. Notably, the beam length for flexural effect is the half length of the shunt sheet span [18], since the centre of the shunt sheet is still horizontal without a deflection angle.

$$\frac{FH^2}{2E_c I_c} = \frac{M_s L}{E_s I_s} \quad (12)$$

The estimated bending moment $M_s = FH/L$ can cause considerable warping deformation and extra strain on the thin shunt sheet surfaces. The maximum strain ε_w due to warping is found at the centre of the shunt sheet,

$$\varepsilon_w = \left(\frac{b}{L} \right) M_s = \frac{bFH^2}{2L I_s E_s} \quad (13)$$

Once the warping angle is calculated, the x-axis displacement of the shunt sheet $\delta_{x,w}$ incurred by warping is derived. The shunt sheet is deformed into an arc shape with length L and angle θ_s to the horizontal on each end.

$$\delta_{x,w} = \left(\frac{\tan\theta_s - \sin\theta_s}{\theta_s} \right) L \approx \frac{\theta_s^2}{2} L \quad (14)$$

$\delta_{x,w}$ is one order minimal value of δ_c , therefore, its impact on the averaged shunt ratio is neglected.

Meanwhile, the bending moment M_s can increase the supporting cantilever's deflection.

$$\delta_c = \frac{FH^3}{3E_c I_c} + \frac{M_s H^2}{2E_c I_c} \quad (15)$$

According to equations (5) and (7), equation (1) can be rewritten into,

$$2(1 + r_c) \left(\frac{FH^3}{3E_c I_c} + \frac{M_s H^2}{2E_c I_c} \right) + \frac{LF}{A_s E_s} = \delta_i = L\varepsilon_i = \frac{1}{r_s} \frac{LF}{A_s E_s} \quad (16)$$

Given the shunt structure is made of single piece of metal sheet, the elastic modulus, thickness and wideness of the metal material are identical. The shunt ratio can be determined by the geometry of shunt structure, independent of the material.

$$r_s = \frac{\frac{L}{A_s E_s}}{2(1+r_c)\left(\frac{H^3}{3E_c I_c} + \frac{FH^3}{2LE_c I_c}\right) + \frac{L}{A_s E_s}} = \frac{Lb^2}{8(1+r_c)\left(1 + \frac{3H}{2L}\right)H^3 + Lb^2} \quad (17)$$

The analytical derivation shows the shunt ratio is independent of target surface material properties and tensile/compressive force on the shunt sheet, assuming rigid connection between the supporting cantilevers to the target surface. In practice, the material of shunt sheet structure should have the similar thermal expansion coefficient, thus the impact of thermal variation target surface can be minimized.

The warping deformation of the shunt sheet leads to the different strain level on the upper and lower surfaces. The shunt ratios based on the strain at the centre of the upper or lower surface can be derived, and they are independent from the strain on the target surface to be measured.

$$\begin{aligned} r_{s,upper} &= r_s \left(1 - \frac{\varepsilon_w}{\varepsilon_s}\right) = r_s \left(1 - \frac{bA_s E_s H^2}{2L I_c E_c}\right) = r_s \left(1 - \frac{6H^2}{Lb}\right) \\ r_{s,lower} &= r_s \left(1 + \frac{\varepsilon_w}{\varepsilon_i}\right) = r_s \left(1 + \frac{bA_s E_s H^2}{2L I_c E_c}\right) = r_s \left(1 + \frac{6H^2}{Lb}\right) \end{aligned} \quad (18)$$

Since the metal sheet thickness b is much smaller than the height of the shunt structure H , the shunt $r_{s,upper}$ can have opposite sign with the averaged shunt ratio r_s . In the practical application, only one shunt ratio is necessary to represent the strain level on the target surface. The lower surface is preferred, since the shunt surface served as a physical shelter for the shunt strain gauge, protecting the gauge from weathering and other kind of physical damage. Alternatively, the lower and upper gauges can form a half-bridge configuration to effectively compensate the temperature induced strain. Furthermore, a strain gauge can be installed beneath the shunt structure for the purpose of the shunt ratio calibration.

D Strain Shunt under Purely Bending Load

According to Fig. 1(c), the purely bending force does not change the length of the neutral plane of the beam, and surface strain is proportionally to the distance to the neutral plane $h/2$ and deflection angle θ . Thereby, the deformation on the bar surface δ_i is less than δ_{shunt} the potential total deformation of the shunt structure at the height of H , see equations (19-20).

$$\delta_i = L\varepsilon_i = \theta \frac{h}{2} \quad (19)$$

$$\delta_{shunt} = 2 \frac{FH^3}{3E_c I_c} \left(1 + \frac{3H}{2L}\right) + \frac{LF}{A_s E_s} \leq \theta \left(\frac{h}{2} + H\right) \quad (20)$$

Furthermore, the shunt ratio based on the averaged strain on upper and lower surface centres of the shunt sheet can be predicted as equation (21).

$$r_b = \frac{\frac{L}{A_s E_s} \left(1 + \frac{2H}{h}\right)}{2 \left(\frac{H^3}{3E_c I_c} \left(1 + \frac{3H}{2L}\right) + \frac{L}{A_s E_s}\right)} \leq \left(1 + \frac{2H}{h}\right) r_s \quad (21)$$

Compared with the purely tensile load, the extra deformation of $H\theta$ results in a larger shunt ratio r_b . The maximum shunt ratio magnification factor of $\left(1 + \frac{2H}{h}\right)$ is based on the assumption of angle constancy at the bottom and top of the supporting cantilever. However, these angles

tend to change under load, hence the magnification factor should be correctly via experimental and numerical study.

E Dynamic Response

For structure under dynamic load, it is required that the harmonic frequency of the shunt structure needs to be significantly higher than that of the target structure. For the target beam structure with the strain shunt structure, the natural frequency under tensile load at one end and fixed at the other end can be predicted theoretically [19].

$$f_1 = \frac{k^2}{2\pi} \sqrt{\frac{EI}{Lb^4 \rho_l}} \quad (k = 1.875 \text{ for the first natural frequency}) \quad (22)$$

where f_i is the characteristic frequencies and E is the elastic modulus and Lb is the length of the bar; ρ_l is the line density of beam. Since large strain level is commonly found on structure with large dimension, its harmonic frequency is lower than that of the tiny strain shunt structure. Thereby, the large dynamic strain below the first natural frequency on the target surface is measured precisely.

III EXPERIMENTAL VALIDATION

A Experimental Setup

Schematic of strain shunt load test setup is shown in Fig. 2; both tensile load and bending load configurations are investigated experimentally. The dimension of the ASTM 1045 carbonate steel bar under the non-destructive tensile test has a dimension $19.7 \times 70.0 \times 1000$ mm. The tensile test is experimentally validated on Tinus Olsen MOM35 tensile test facility, as demonstrated in Fig. 2 (a). Furthermore, bending load is tested with static and dynamic load, as illustrated in Fig. 2 (b). The smaller bar made of carbonate steel ASTM 1045 with a dimension of $3.1 \times 25.0 \times 614$ mm is designed for bending load tests. Several weight units are hanged at one end with the other end fixed. In addition, another bending configuration is set up with balanced loads on both ends of the test bar, shown in Fig. 2 (c).

Two strain shunt structures of the same geometry are bonded to the target bar material for the tensile and bending load tests respectively. The tensile test is carried out on a larger beam material, to minimise the impact of undesired bending load during clamping. The strain shunt structures are made of steel sheet with a thickness $b=0.90$ mm. The average height the shunt sheet H is about 11.0 mm (varying from 10.8 to 11.2 mm), and the span of the shunt sheet is $L=52$ mm. This strain shunt structure is made by the metal sheeting process, which is convenient to manufacture and install. The inner fillet radius is controlled as 0.5 mm for the joint of cantilever and shunt sheet and 2.1 mm at the binding feet. The shunt structure is bonded onto the target bar surface by AE10 epoxy resin adhesive.

Two metal foil strain gauges of Vishay C2A-06-125LW series are installed on the lower and upper surface centres of the shunt sheet, shown as SA1 and SA2 respectively in Fig. 3. Another strain gauge (SA0) is installed onto the bar under load test; this gauge measurement is compared with the reduced strain on the shunt structure, i.e. SA1 and SA2. Dimension of the effective gauge grid is 1×2 mm for this type of strain gauge, while the overall dimension is 2×4 mm with extra area for binding. Limited by the width of the shunt

sheet, only one such commercial-off-the-shelf strain gauge is installed on each side of the shunt sheet. However, quarter-bridge is regarded as sufficient for the strain gauges in the constant temperature laboratory environment. In practice, half-bridge or full bridge should be used to compensate temperature induced variation. The voltage signal from the strain gauges is amplified and digitalised by the wireless sensor network strain gauge module NI-WSN 3214 supplied by National Instruments, which has a high analogue to digital conversion resolution of 20 bits. Finally, the digitalised voltage signal is gathered by the Ethernet gateway NI-WSN 9791 for further data processing. At least 200 samples have been recorded for each static load case, at a sampling rate of 40 samples per second. The temporal standard variation of strain measurement is well controlled as $1 \mu\epsilon$.

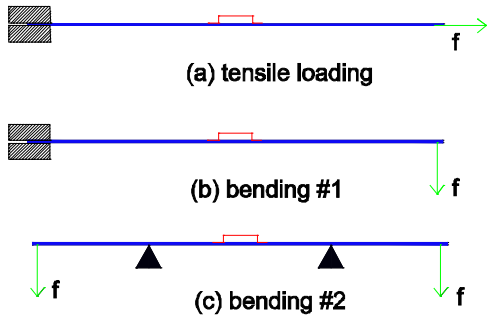


Fig. 2 Schematic of various load test configurations.

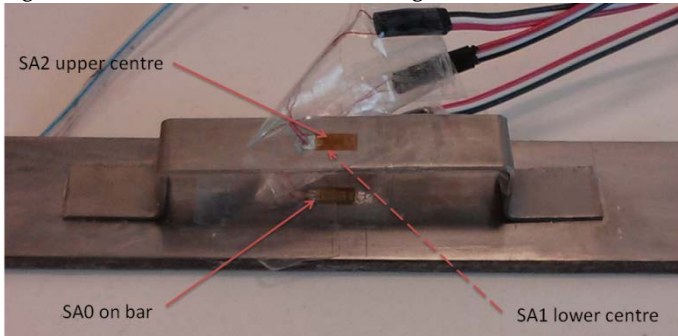


Fig. 3 Shunt structure under bending loads and gauge positions.

B Tensile Load Test

The strain level in the tensile load experiment is shown in the Table 1. No plastic deformation is confirmed by no residual strain after the load test, shown in Table 1. As it is difficult to maintain the desired load for the first three load points, the first three cases are excluded for large deviation from the theoretical prediction of strain on bar. The averaged shunt ratio based on the strain at the lower surface centre is 0.069, while the analytical solution gives 0.051 for the simplified 1D model. The under-estimated shunt ratio is attributed to neglecting the fillet structure in the 1D model and the approximation of angle constancy in Eq. (9). However, this theoretic analysis provides reasonable estimation of the shunt ratio, based on the primary geometrical parameters, such as shunt height, sheet thickness.

C Purely Bending Load Test

Strain shunt has been tested on a smaller bar with one end fixed and hanging weight on the other end, shown in the load configuration of Fig. 2 (b). X-axis normal strain on upper surface centre (SA2) and that on lower surface centre of the

shunt sheet (SA1), are compared with the strain on the bar surface beneath the shunt structure (SA0). The excessive deformation of the supporting cantilever results in significant bending moment at the joints, which leads to observable warping of the shunt sheet. Due to the large ratio of span to thickness, the warping effect dominates the strain distribution on the shunt sheet. Therefore, the strain on the upper surface of the shunt sheet is of opposite sign with the load on the bar surface. Furthermore, the shunt ratios $r_{s_lower} = 0.213$ and $r_{s_upper} = -0.156$ (standard deviations are 0.00234 and 0.00235 respectively) are not significantly affected by this large deflection phenomenon, and a constant relationship between the strain on bar (SA0) and strain at the shunt sheet can be obtained, see Fig. 4.

Table 1 Averaged strain and shunt ratio for tensile load test

Load force (kN)	Theoretical solution ($\mu\epsilon$)	Strain on bar SA0 ($\mu\epsilon$)	Strain at SA1 ($\mu\epsilon$)	Shunt ratio
0	0	0.8	-1.7	N.A.
50	175.5	133	10.912	0.08205
100	351	316	24.728	0.07825
150	526.5	456	34.584	0.07584
200	702	682	46.904	0.06877
250	877.5	854	58.96	0.06904
300	1053	1030	70.576	0.06852
350	1228.5	1210	82.984	0.06858
400	1404	1380	95.744	0.06938
450	1579.5	1550	107.976	0.06966
500	1755	1740	119.768	0.06883
450	1579.5	1592.5	107.624	0.06758
400	1404	1402.2	94.776	0.06759
350	1228.5	1229.0	83.336	0.06781
300	1053	1050.1	71.104	0.06771
250	877.5	876.6	59.576	0.06796
200	702	701.3	47.6256	0.06791
150	526.5	522.3	35.4728	0.06792
100	351	346.5	23.848	0.06883
50	175.5	172.0	12.232	0.07112
0	0	-0.9	0.6	N.A
Averaged shunt ratio r_{s_lower} :				0.069

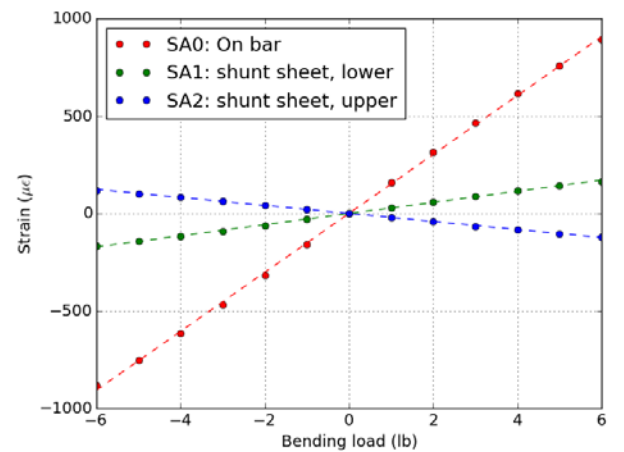


Fig. 4 Validation of linearity of strain shunt under bending at one end.

The shunt ratio is independent of the tested bending load configurations, as shown in Fig. 2 (b-c). The second bending test has been carried out with symmetric load on the both end, illustrated as the bending configuration 2 in Fig. 1 (d). Since the deflection angle at the centre of the bar is zero for the symmetrical bending load, this configuration is less concerned for the error from large deflection. The shunt

ratios based on strain at the upper and lower surface centre is -0.148 and 0.210 respectively; the shunt ratio based on the strain gauge on the shunt sheet lower surface agrees with that of the first bending configuration, i.e. 0.213. These shunt ratios are about 1.6% smaller than those of bending configuration 1, but this deviation falls in range of the standard deviation of 0.0063. Especially, the shunt ratio based on the strain gauge on the shunt sheet upper surface is subjective to nonlinear error, i.e. a trend of increasing shunt ratio with the bending load, see Table 2.

On the other hand, significant error is found in theoretical prediction of shunt ratio for bending load. The theoretical analysis gives -0.35 and 0.40 for shunt ratios on the upper and lower surface centre respectively, according to the derived amplification ratio $(1+2H/h)$ in Eq. (21). Meanwhile, the bending load experiments indicate 0.031 as an average of -0.148 and 0.210, shunt ratios for the upper and lower surface centre respectively. There is a distinct gap between analytical prediction and experimental result. It is suggested that the assumption of angle constancy at the fillet transition has significant error for the case of bending load, but the shunt ratio for bending load may be predicted analytically via an empirical correction ratio.

For the strain gauge at the centre of the lower surface (SA1), the averaged shunt ratio for purely tensile load is 0.069 for tensile load (see Table 1). However, the shunt ratio for purely bending load is 0.213, much higher than that of the tensile load. According to equation (17) and (21), the difference in the shunt ratio is caused by the large ratio of shunt height H to the distance of the target surface to neutral plane $h/2$, for the current experimental setup. For the practical application of strain shunt in large dynamic strain measurement, the shunt height H could be ignored, compared to the thickness the half-width of the target large dimension structure e.g. wind turbine tower. Furthermore, the geometry of the strain relieving unit can be redesigned as Ω -shaped bend cantilever instead of I-shaped cantilever, which can lower the shunt sheet adjacent to the target surface as possible. Thereby, the difference in shunt ratio for bending load or tensile load is minimal.

D Dynamic Load Test

The dynamic response of the strain shunt is tested by dynamic bending load, and the constancy of shunt ratio is confirmed by the temporal response in Fig. 5. For the bending load configuration #1, bending force has been manually loaded three times with an interval of 1 second, then the test bar is left damping in the air. The red line represents the strain level on the target surface underneath the shunt (SA0); the green line is the strain at the shunt sheet lower surface centre (SA1). The blue points in Fig. 5 are the strain value on shunt sheet bottom surface divided by the shunt ratio 0.213 obtained from the bending load test. For the three pulse load periods, the calculated strain agrees well with measured strain beneath the target bar, but the strain is slightly over-estimated by the shunt ratio if the strain is low during the free damping process.

The applicability of shunt ratio to dynamic strain up to 40 Hz is confirmed in Fig. 5. The theoretic resonant frequency of

cantilever for the bending load without damping is given by Eq. (22) [19]. For the steel bar under bending test, the first natural frequency for a cross-section of 3.1×25 mm bar is about 48 Hz. Due to the significantly smaller cross-section area (0.9×10.8 mm) of the shunt sheet and the existence of supporting cantilevers, the first characteristic frequency is 167 Hz (given by FEA modal analysis with one foot surface fixed and the other free in Z-axis), which is significantly higher than the target bar structure. Therefore, the shunt structure has a much higher first characteristic frequency; and dynamic strain on the target surface under large dynamic load below the resonance frequency can be captured, e.g. 1Hz forced actuation in this experimental evaluation.

Table 2 Temporal averaged strain for bending load configuration 2

Bending load (lb)	Strain on bar SA0 ($\mu\epsilon$)	Strain at SA1 ($\mu\epsilon$)	Shunt ratio, lower	Strain at SA2 ($\mu\epsilon$)	Shunt ratio, upper
-10.00	-901.34	-189.38	0.210105	138.21	-0.15334
-9.00	-812.07	-171.72	0.211464	124.46	-0.15327
-8.00	-722.97	-153.24	0.211953	110.29	-0.15256
-7.00	-632.80	-134.19	0.212054	95.67	-0.15119
-6.00	-541.80	-115.42	0.213035	81.62	-0.15065
-5.00	-450.09	-96.61	0.214649	67.50	-0.14998
-4.00	-360.45	-77.83	0.215912	53.44	-0.14826
-3.00	-269.90	-58.91	0.218265	39.24	-0.14537
-2.00	-177.78	-39.36	0.221385	24.92	-0.1458
-1.00	-90.02	-20.20	0.224431	11.14	-0.14597
1.00	90.67	18.17	0.200418	-10.39	-0.14769
2.00	186.56	37.23	0.199553	-24.33	-0.14112
3.00	273.22	56.19	0.205651	-38.25	-0.14001
4.00	364.56	75.08	0.205931	-52.04	-0.14276
5.00	454.35	93.95	0.206777	-66.09	-0.14545
6.00	552.81	113.11	0.204611	-80.47	-0.14556
7.00	638.90	132.24	0.206984	-94.94	-0.1486
8.00	728.39	151.39	0.207838	-109.50	-0.15033
9.00	818.30	170.95	0.208906	-124.21	-0.15179
10.00	896.39	189.38	0.211265	-138.21	-0.15419
Averaged shunt ratio:			0.210		-0.148

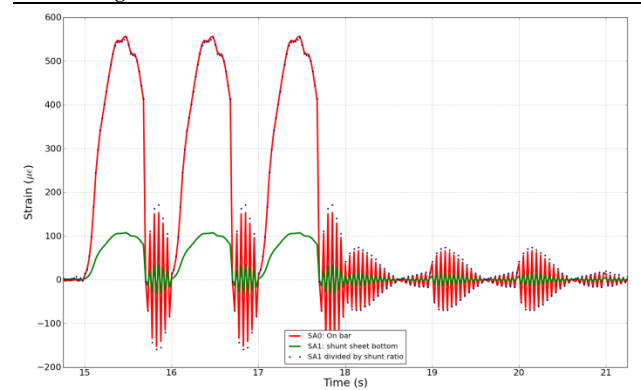


Fig. 5 Dynamic response of strain shunt for impulsive bending load configuration.

IV NUMERICAL ANALYSIS

Due to the limitation of the load test facility, a few interesting topics can not be studied via experiment, for example, the response to compound load and stress concentration. The complementary numerical analysis is conducted on the finite element analysis software, Ansys Mechanical version 14.0.

A Numerical Model Validation

The bending load configuration and boundary condition are described for the 3D finite element model. Firstly, fixed support is selected for the clamping fixture at one end; and uniform surface force load is applied on the other end. Secondly, the thin adhesive layer is modelled as “bonded” type to simulate the non-separate and non-sliding joint conditions between the shunt structure and the target bar. The adhesive layer with thickness 0.1 mm is modelled with an elastic modulus of 3.5 GPa. Thirdly, the fillet radius at the shunt feet is measured as 2.1 mm.

Mesh independent check is conducted on three meshes with 85032, 214560 and 532684 elements. The medium mesh density is regarded sufficient for this numerical study, since strain difference is less than 0.3% different from the fine mesh. Furthermore, this numerical model is validated by the theoretical solution of tensile strain on the bar. Correctness of the FEA model can be confirmed by the agreement of strain level on the target bar surface from theoretical solution for the tensile load test and simulation. On the other hand, 2.5% difference is observed for the strain at SA0 for 2 pound bending load (bending load configuration #1), corresponding to bending force $f_b = 8.9$ N in Table 4. The positional deviation of strain gauge installation and load force contributes to this difference, while reasonable accuracy is achieved for the stress concentration and geometrical sensitivity study.

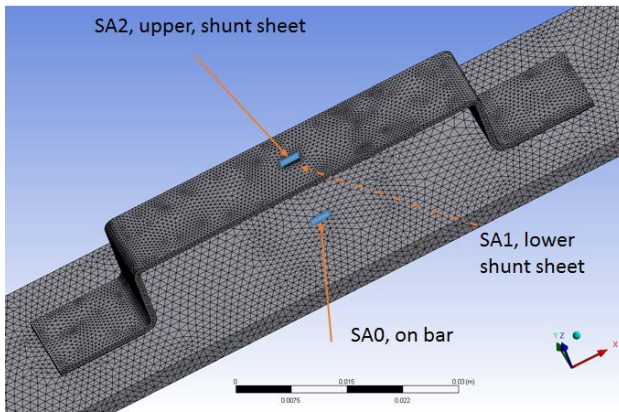


Fig. 6 The medium mesh for strain shunt design with train gauge position

B Investigation of Compound Load

The shunt ratio calculated by the FEA model matches experiment data. The shunt ratio $r_{s_lower} = 0.069$ by experiment for tensile load agrees with the FEA result of 0.0689. On the other hand, the bending force shunt ratio is $r_{b_lower} = 0.213$ by experiment, which is smaller than the numerical evaluation of 0.2199. The 3.2% difference in shunt ratio is attributed to geometrical error during manufacturing and installation, measurement uncertainty and numerical model simplification.

Table 3 X-axis normal strain for different load combination

Case	f_t (kN)	f_b (N)	Strain on bar, SA0 ($\mu\epsilon$)	Strain, SA1 ($\mu\epsilon$)	Shunt ratio, lower	Strain, SA2 ($\mu\epsilon$)	Shunt ratio, upper
Exp.	0	-8.9	317.14	67.62	0.2132	-50.57	-0.1595
1	0	-8.9	-325.6	-71.6	0.2199	50.3	-0.1545
2	0	8.9	325.4	71.6	0.2200	-50.2	-0.1544
3	10	0	641.3	44.2	0.0689	-37.2	-0.0580
4	10	-8.9	966.8	115.8	N.A.	-87.3	N.A.

5	10	8.9	315.5	-27.4	N.A.	13.2	N.A.
6	10	0	641.3	44.2	0.0689	-37.2	-0.0580
7	0	8.9	313.83	67.97	0.2199	-49.17	-0.1567

Note: shunt ratio does not apply (N.A.) to the combination of tensile and bending load.

Compared with the conventional metal foil strain gauge, one of the drawbacks of the strain shunt is that the bending and tensile load leads to different the shunt ratio, if the shunt height can not be ignored with respect to the target structure dimension. The difference in the shunt ratio results in inconvenience during measurement of complex load, for example, the combination of tensile load and purely bending load at one end and fixed at the other end in this numerical study. It is not possible to distinguish the contribution of either bending or tensile load by single strain shunt structure. However, half bridge configuration of two strain shunts can solve this problem, given both shunt ratios are stably linear. By installing two strain shunt structure at proper positions, e.g. the opposite surface of the target beam structure, just as two strain gauges in a half bridge configuration; the compressive or tensile load can be derived from complex load. For example, averaging the case of $f_t = 10000$ N and $f_b = 8.9$ N with the case $f_t = 10000$ N and $f_b = -8.9$ N leads to the strain value for the pure tensile load $f_t = 10000$ N. Similarly, subtracting these two cases results in the identical strain distribution on the shunt structure under pure bending force, shown in Table 4.

C Evaluation of Stress Concentration

Numerical study shows the stress concentration has been relieved significantly, compared with the column-sheet assembly design with the cantilevers welded onto the target surface. Fig. 7 illustrates the von-Mises stress contour on the shunt structure. The maximum stress of 152 MPa on the shunt is found the fillet transition from the binding feet to the supporting cantilever. The maximum stress is found near the binding foot, but it is 10% less than the stress on the target bar surface beneath the shunt structure (SA0), under purely bending force 22.2 N at one end. Therefore, the shunt structure is less concerned for failure before the target structure, assuming the strain shunt structure is made of the same steel material.

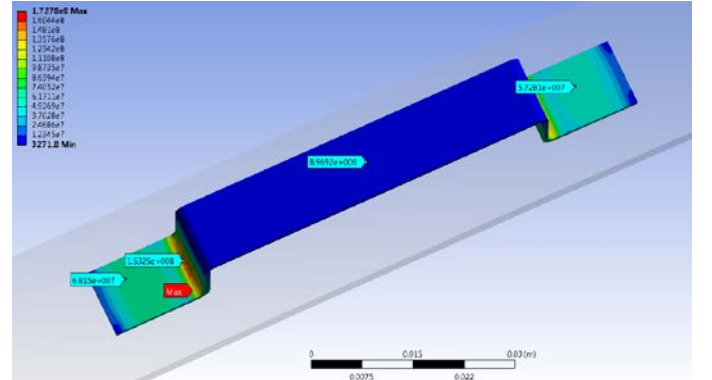


Fig. 7 Stress contour of for equivalent (von-Mises) stress on strain shunt ($f_b = 22.2$ N)

Given the identical material for the target structure and the attached shunt structure, shunt sheet will not fail before the target surface with respect to fatigue failure. However, the fatigue failure of the shunt structure fixture/fastening is a major concern for deployment. The current tested setup

utilizes the adhesive to bond the shunt structure to the target surface. The failure of bonding via weathering, corrosion, fatigue is a major concern for the strain shunt structure, which is worth of further investigation. Alternative solutions could be shunt sheet welding, threading fixture, etc.

V CONCLUSION

In this paper, a strain shunt structure which reduces the large dynamic strain level proportionally to a safe level has been proposed and validated experimentally. The working principles of strain shunt design are illustrated and shunt ratio is derived analytically from a simplified 1D model. The prototype structure of a shunt sheet bridging two supporting cantilever beams aims to reduce the stress concentration and ease the installation.

This design has been validated through tensile and bending test for both static and dynamic load. Constant shunt ratio of strain measured on the shunt sheet to that on the target surface is observed for either purely tensile or purely bending load, and the shunt ratio agrees with the analytical prediction based on the 1D model. Furthermore, the numerical study also confirms the fillet of the metal sheet can relieve stress concentration efficiently.

REFERENCES

- [1] M. D. C. Segovia Garcia, M. J. T. Revie, and F. Quail, "Condition monitoring data in the study of offshore wind turbines' risk of failure," 2013.
- [2] C. C. Ciang, J.-R. Lee, and H.-J. Bang, "Structural health monitoring for a wind turbine system: a review of damage detection methods," *Measurement Science and Technology*, vol. 19, p. 122001, 2008.
- [3] A. Hamilton and F. J. Quail, "Detailed state of the art review for the different on-line/in-line oil analysis techniques in context of wind turbine gearboxes," *Journal of Tribology*, vol. 133, 2011.
- [4] V. Micro-Measurement, "Introduction to Stress Analysis by the PhotoStress® Method," Vishay Tech Note TN-702-22005.
- [5] V. Micro-Measurements, "Strain Gage Selection: Criteria, Procedures, Recommendations," Tech Note TN-5052007.
- [6] T. K. B. Günther, Ed., *Optical versus electrical strain gages: A comparison*. HBM Measurements, 2007, p. ^pp. Pages.
- [7] J. Roths, A. Wilfert, P. Kratzer, F. Jülich, and R. Kuttler, "Strain calibration of optical FBG-based strain sensors," in *(EWOFs'10) Fourth European Workshop on Optical Fibre Sensors*, 2010, pp. 76530F-76530F-4.
- [8] S. Yang, B. Zhou, T. Sun, and K. T. Grattan, "A Novel Optical Sensor Platform Designed for Wireless Sensor Networks," in *Journal of Physics: Conference Series*, 2013, p. 012007.
- [9] D. Ryu, F. N. Meyers, and K. J. Loh, "Inkjet-printed, flexible, and photoactive thin film strain sensors," *Journal of Intelligent Material Systems and Structures*, vol. 26, pp. 1699-1710, 2015.
- [10] M. Komachiya, R. Minamitani, T. Fumino, T. Sakaguchi, and S. Watanabe, "Proof-testing and probabilistic lifetime estimation of glass fibers for sensor applications," *Applied optics*, vol. 38, pp. 2767-2774, 1999.
- [11] J. Sirohi and I. Chopra, "Fundamental understanding of piezoelectric strain sensors," *Journal of Intelligent Material Systems and Structures*, vol. 11, pp. 246-257, 2000.
- [12] B. Pan, K. Qian, H. Xie, and A. Asundi, "Two-dimensional digital image correlation for in-plane displacement and strain measurement: a review," *Measurement Science and Technology*, vol. 20, p. 062001, 2009.
- [13] W. Steinchen and L. Yang, *Digital shearography: theory and application of digital speckle pattern shearing interferometry*. SPIE press Bellingham, 2003.
- [14] X. Qingfeng and Y. Longyang, "Inductive wireless charging and pulse energy harvesting for wireless sensor on rotating machine," *Wireless Power Transfer*, vol. 3, 2016.
- [15] Q. Xia and F. Quail, "Principles and validation of strain gauge shunt design for large dynamic strain measurement," *Sensors and Actuators A: Physical*, vol. 241, pp. 124-134, 2016.
- [16] O. Bauchau and J. Craig, "Euler-Bernoulli beam theory," in *Structural Analysis*, ed: Springer, 2009, pp. 173-221.
- [17] C. E. Augarde and A. J. Deeks, "The use of Timoshenko's exact solution for a cantilever beam in adaptive analysis," *Finite Elem. Anal. Des.*, vol. 44, pp. 595-601, 2008.
- [18] R. C. Juvinall and K. M. Marshek, *Fundamentals of machine component design*, 4th ed.: J. Wiley (New York), 2006.
- [19] S. G. Kelly, *Mechanical Vibrations: Theory and Applications*: Cengage Publishing, 2012.

Prof Tieyu Gao obtained his Ph.D from Xi'an Jiaotong University in June 2003. Currently, he is an associate professor at the school of Energy and Power Engineering, Xi'an Jiaotong University. His research focuses on the flow and heat transfer mechanism in gas turbine and steam turbine, two-phase flow separation and the steam moisture monitoring technology.

Dr Qingfeng Xia obtained his PhD in Aerospace Engineering from the University of Manchester in March 2012. Currently, he is a research associate at the Department of Engineering Science, the University of Oxford. His research interests include flow visualization, condition monitoring, sensor design and Multiphysics modelling.